

communications

earth & environment

ARTICLE



<https://doi.org/10.1038/s43247-021-00133-7> OPEN

Dipole patterns in tropical precipitation were pervasive across landmasses throughout Marine Isotope Stage 5

Katrina Nilsson-Kerr^{1,5}✉, Pallavi Anand¹, Philip B. Holden¹, Steven C. Clemens² & Melanie J. Leng^{3,4}

Most of Earth's rain falls in the tropics, often in highly seasonal monsoon rains, which are thought to be coupled to the inter-hemispheric migrations of the Inter-Tropical Convergence Zone in response to the seasonal cycle of insolation. Yet characterization of tropical rainfall behaviour in the geologic past is poor. Here we combine new and existing hydroclimate records from six large-scale tropical regions with fully independent model-based rainfall reconstructions across the last interval of sustained warmth and ensuing climate cooling between 130 to 70 thousand years ago (Marine Isotope Stage 5). Our data-model approach reveals large-scale heterogeneous rainfall patterns in response to changes in climate. We note pervasive dipole-like tropical precipitation patterns, as well as different loci of precipitation throughout Marine Isotope Stage 5 than recorded in the Holocene. These rainfall patterns cannot be solely attributed to meridional shifts in the Inter-Tropical Convergence Zone.

¹Faculty of STEM, School of Environment, Earth and Ecosystem Sciences, The Open University, Milton Keynes, UK. ²Department of Geological Sciences, Brown University, Providence, RI, USA. ³National Environmental Isotope Facility, British Geological Survey, Nottingham, UK. ⁴School of Biosciences, University of Nottingham, Loughborough, UK. ⁵Present address: The Lyell Centre, Heriot-Watt University, Edinburgh, UK. ✉email: k.nilsson-kerr@hw.ac.uk

The hydrological cycle is expected to intensify as Earth warms, owing to increased moisture availability (following the Clausius–Clapeyron equation)¹. Of crucial importance is an accurate projection of precipitation change in tropical regions (30°N–30°S), where dense human populations live with intimate socioeconomic links with climate. The majority of Earth's rain falls in the tropics and in some regions it is highly seasonal (e.g., the monsoons), being coupled to the inter-hemispheric migrations of the Inter-Tropical Convergence Zone (ITCZ) in response to the seasonal cycle of insolation. Therefore, the tropical precipitation forms an integral part of the global climate system. Yet, despite both its regional and global significance, the response of rainfall to future climate has been proven challenging to predict² and there remains a poor characterization of rainfall in the geologic past. Reconstructions of past rainfall are limited by an unequal spatial and temporal coverage of proxy records, augmented by chronological uncertainties. Moreover, the principal challenge in gaining an accurate quantification of past rainfall amount resides in the capacity of geochemical climate proxies to faithfully record a single, specific climate variable of interest³ (e.g., local rainfall amount). Paleoclimate records inferring past rainfall variability have nevertheless typically converged on attributing changes in precipitation to fluctuations in the meridional position of the ITCZ, with the ITCZ position across the Late Pleistocene primarily being regulated by insolation, Northern Hemisphere ice-sheet size and/or alterations of the oceanic overturning circulation^{4–6}. A notable example is the identified antiphase trend between speleothem oxygen isotope ($\delta^{18}\text{O}$) records from China with those in South America during periods of Northern Hemisphere cooling and warming⁷. Attributing north–south ITCZ shifts have seemed a sufficient explanation for describing tropical paleoclimate variability given that the ITCZ is sensitive to energy fluxes, and thus ice-sheet build-up in the northern hemisphere should be associated with a parallel decrease in tropical precipitation in the same hemisphere⁸. More recently, however, the view of large-scale uniform shifts of the ITCZ position for determining past rainfall responses has been cast into doubt by modelling studies, suggesting variable regional^{9,10} and minimal observed meridional ITCZ movements despite applying significant climate forcing¹¹. Regional contractions and expansions of the tropical precipitation belt have been inferred for the late Holocene, based on some proxy studies, as better depicting the nature of past rainfall changes rather than a simple uniform meridional shift of the ITCZ in response to past climate forcings^{12,13}. This suggested regional heterogeneity in tropical precipitation highlights the rapidly increasing spatial coverage of proxy records. This has resultant implications on understanding of the “Global Monsoon”, a concept that links the regional monsoon systems (seasonal rainfall affecting large parts of Asia, Africa, Australia and the Americas) in an attempt to convey their collective sensitivity to the annual cycle of solar radiation and atmospheric overturning circulation¹⁴. Thus, application of this concept in past monsoon rainfall reconstructions may be inadequate due to its inability to encapsulate the potential diversity in the response of each regional monsoon system to climate forcing¹⁵.

There have been meaningful and successful attempts within the paleoclimate community to compile global and large-scale regional records of sea surface temperatures (SSTs) across various time periods in the past^{16–18}, although equivalent studies of past rainfall have largely remained limited^{19,20}. To depict the evolving characteristics of geographic variations of rainfall to past changes in climate, a greater geographic coverage of proxy records and more integrated approaches are needed¹⁹. Here we investigate transient tropical past hydroclimate variability in context to the “Global Monsoon” during the warm interval of Marine Isotope

Stage (MIS) 5 (130–70 ka) by combining newly generated proxy records of the Indian Summer Monsoon (ISM) from the core ISM rainfall region of the Bay of Bengal (Methods and Fig. 1) with existing paleoclimate records that are inferred to capture hydroclimate (Methods). We employ the broad term hydroclimate to encompass the various nuances in paleoclimate approaches to reconstruction of “wet” or “dry” past environments. To evaluate the robustness of these signals, Fig. 2 compares the proxy records with fully independent reconstructions of precipitation that are derived from PaleoPGEM²¹, a spatiotemporal emulator of the intermediate-complexity atmosphere–ocean GCM PLASIM-GENIE²². Although investigations to capture a specific time snapshot using high-resolution equilibrium simulations¹⁹ are useful, our approach, which explores past hydroclimate using a time series of hydroclimate emulations at intermediate resolution with uncertainty quantification, permits a more holistic assessment of the behaviour of the tropical rain belt in response to evolving climate forcing.

Results and discussion

We have employed a simple approach of allocating “wetter” and “drier” conditions relative to the mean signal (across the study interval, 70–130 ka), to present a diverse suite of tropical multi-proxy records in a unified manner for comparison (Fig. 2) (Methods). These tropical multi-proxy records, inferred to capture past hydroclimate, include various caveats in their ability to accurately record past hydroclimate associated with measurement (instrument/user) and calibration errors in addition to the interpretation of the reconstructed signal, of which the latter is by far the largest source of uncertainty. Furthermore, these records are predominantly confined to capturing a terrestrial rainfall signal owing to the nature of sample locations (Fig. 1). However, the collations of the available proxy-based hydroclimate records show a relative consistency among themselves and with the model-based (yellow line, Fig. 2) average precipitation record across MIS 5 (Fig. 2). This evidence for regional wetting and

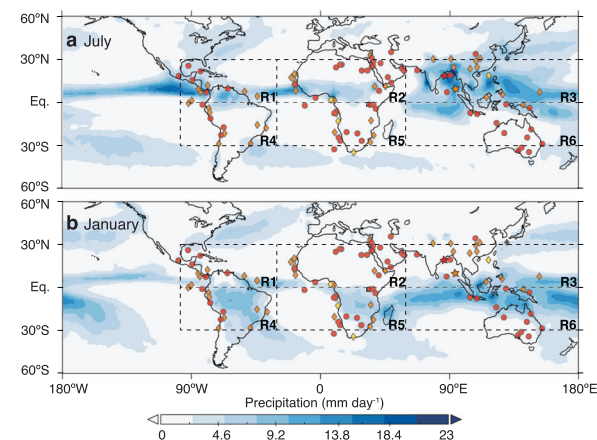


Fig. 1 Present-day tropical precipitation. Map showing mean (1981–2010) CMAP global precipitation¹²¹ rates during July (a) and January (b), conveying seasonal ITCZ migration and monsoonal development. Gridded boxes highlight tropical division of Regions 1 through to 6. Orange diamonds represent proxy records used for both time series and anomaly-map comparisons (Figs. 2 and 3), yellow diamonds represent proxy records used only for time series (Fig. 2), red circles represent proxy records used only in the anomaly map (Fig. 3) and stars represent proxy records generated in this study (red, U1446 and orange, U1448) (see Methods and Supplementary Data 1 for detail and references). Precipitation data available from <https://psl.noaa.gov/data/gridded/data.cmap.html>. Map produced using Panoply (source: <https://www.giss.nasa.gov/tools/panoply/>).

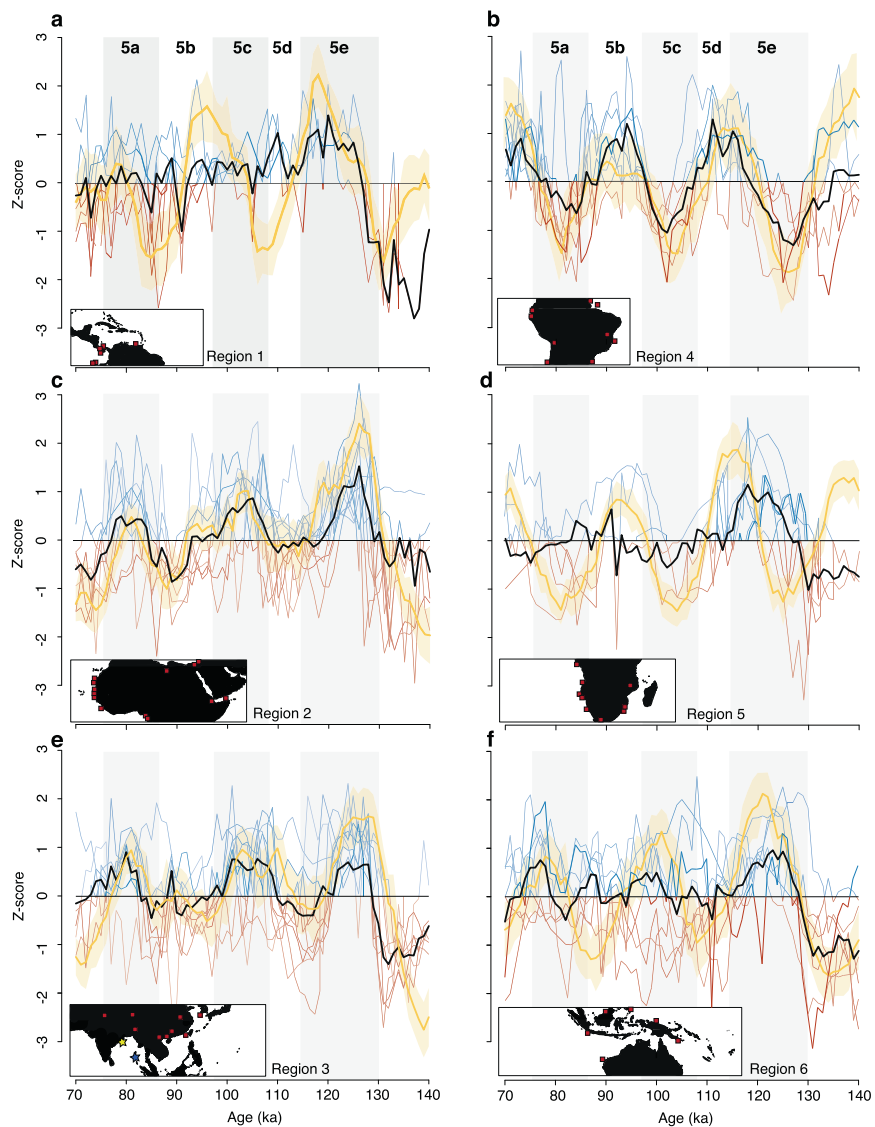


Fig. 2 Hydroclimate reconstructions across Marine Isotope Stage 5. Time-series proxy and average emulation signal comparison across the six regions defined by latitude and longitude across MIS 5 **a** Region 1, **b** Region 4, **c** Region 2, **d** Region 5, **e** Region 3 and **f** Region 6. The emulation-derived precipitation is shown in yellow with the lighter yellow shading representing the 95% confidence limit. The black line represents the average of all proxy data in each respective region. The z-scores represent the deviation from the mean of each proxy record, with blue representing “wetter” (more positive z-score) and red “drier” (more negative z-score) conditions. Each plot contains an inset map for each region with red squares for the location of published proxy records and location of the two new records generated in this study are shown as coloured stars (see Methods and Supplementary Data 1). Grey shaded bars represent the warm MIS 5 sub-stages (MIS 5e, c and a).

drying across the warm sub-stages (MIS 5e, c and a) and cooler sub-stages (MIS 5d, b) lends support to the ability of the collated proxy records to capture a representative signal of hydroclimate across MIS 5, in spite of the range of complications associated with each respective proxy record. This is further supported by good coherence found between the collation of our proxy records with a recently published record of the Dole effect (ΔDE^*), proposed as a measure of the low-latitude hydrological cycle²³ (Supplementary Fig. 1). However, deviations between proxy records nevertheless exist at both the orbital and millennial scales (Fig. 2), highlighting the influence of local climate processes, differing sensitivities and time-transgressive responses to boundary conditions²⁴, and complication with the proxy signal itself (Methods). Regions 3 (Fig. 2e) and 6 (Fig. 2f) exhibit clear divergences among the compiled proxy records within each respective region manifested by contemporaneous wetting and drying episodes across MIS 5 (Fig. 2e, f). Region 3 encompasses

the two Asian Monsoon subsystems, the ISM and East Asian Summer Monsoon (EASM), in addition to the maritime continental regions of the Indo-Pacific Warm Pool (IPWP), which also overlaps in Region 6 and further includes the Australian-Indonesian Monsoon. Discrepancies in temporal coupling between the ISM and EASM have been documented at both orbital and millennial scales^{24–27}, and are attributed to the differing sensitivities of these two subsystems to boundary conditions and climatological differences²⁸. The observed discrepancies may also be attributed to the interpretation of the monsoon rainfall signal reconstructed from speleothems in the regions, which remains contentious (Methods). However, the spatio-temporal emulation of Region 3 exhibits a lack of correlation at the local scale (mean correlation of 0.19 between individual grid cells and the regional mean in PaleoPGEM; Supplementary Fig. 2), highlighting that the observed diversity in response to climate forcing in this region captured by the proxy records is

associated with significant local sensitivities to climate forcing. Separation of the proxy records into their respective ISM and EASM-dominated realms (Supplementary Fig. 3) highlights that there is a distinct heterogeneous response of each monsoonal subsystem to climate forcing across MIS 5. Not only is Northern Hemisphere Solar Insolation (NHSI) thought to be a key driver in the monsoonal circulation over the Asian landmass^{29,30} but the effects of sea level³¹, ice volume and greenhouse gas concentrations³² change in Atlantic Meridional Overturning Circulation strength³³ and bi-hemispheric forcing^{24–26,34} are all implicated to exert an influence in dictating past monsoonal strength in the Asian Monsoon regions across glacial–interglacial timescales, although proxy records from the IPWP infer climate to be insensitive to high-latitude forcing in response to a dominance of local insolation forcing^{35–37} or sea-level changes³¹. Thus, the observed deviations among the individual proxy records in Regions 3 and 6 at the millennial scale highlight the complex interplay of regional and local sensitivities in dictating hydroclimate within these realms requiring proxy-based paleoclimate interpretations to recognize these complexities.

In comparison, Regions 1, 2, 4 and 5 (Fig. 2a–d) exhibit a more coherent relationship between the compiled proxy records within each region at the millennial scale with periods of extreme wet/dry conditions akin to the warm/cold sub-stages of MIS 5 being identified. This is further reinforced by a good correlation at the local scale as emulated by PaleoPGEM (Supplementary Fig. 2). Modelling studies have shown that rainfall within the Atlantic Ocean and its margins correlate well with the zonal mean ITCZ^{9,10}. Proxy records from these regions also invoke an intimate link of hydroclimate variations within Central and South America^{5,7}, northern and southern Africa^{38–40} to be linked with meridional ITCZ shifts as a result of changes in the inter-hemispheric Atlantic SST gradient coupled with precession-paced changes in summer insolation⁴ (Supplementary Fig. 4). However, temporal discrepancies between precession, inter-hemispheric heat transport and emulated precipitation do exist across MIS 5 (Supplementary Fig. 4), highlighting the additional importance of local processes in determining hydroclimate variability. The existence of intervals containing limited anti-phasing between

respective regional northern and southern hemisphere records (Supplementary Fig. 5) supports limited hemispheric anti-phasing found in studies from the Holocene^{10–12} and in recent times⁴¹, therefore, underscoring that hydroclimate variability cannot be explained by ITCZ shifts alone.

Meridional and zonal precipitation variability. Figure 3 shows the qualitative values of “wetter” and “drier” assigned to proxy data (blue and red data points, respectively) (Methods), to simplify and further disentangle past patterns in hydroclimate variability that is limited by the transient approach (Fig. 3). Results are shown for each MIS 5 sub-stage with respect to the average Holocene (Methods) and are superimposed on our emulation of spatial rainfall. The results reveal pronounced tropical regional heterogeneities in response to climate forcing across MIS 5 (Fig. 3). Overall, there is good proxy-model data convergence, particularly during both the warmest time-slice MIS 5e (Fig. 3a) and coolest time-slice MIS 5b (Fig. 3e). Discrepancies between the proxy and model anomalies with respect to the Holocene may be the result of the intermediate-resolution nature of the model²¹ (Methods) or due to the various factors associated with the proxies (Methods).

In general, the Southern Hemisphere tropics (0–30°S) experience an intensified rainfall regime during the cooler sub-stages of MIS 5d and b, especially over land masses (Fig. 3d, e), and a reduction in rainfall during the warmer sub-stages (Fig. 3a–c) with respect to the Holocene. This intensification of the Southern Hemisphere tropical hydroclimate is consistent with a shift of the ITCZ southwards (northwards) during cool (warm) Northern (Southern) Hemisphere episodes⁴. Although this hemispheric antiphase pattern in hydroclimate variability across MIS 5 may be associated with ITCZ shifts, it is insufficient for explaining our reconstructed spatial pattern of precipitation, which is coherent from both our proxy collations and emulation (Fig. 3). The modelled precipitation anomalies and proxy data reveal intensified rainfall regimes both north and south of the equator in South America and Africa during MIS 5e (Fig. 3a), whereas distinct zonal wet-dry patterns exist throughout MIS 5

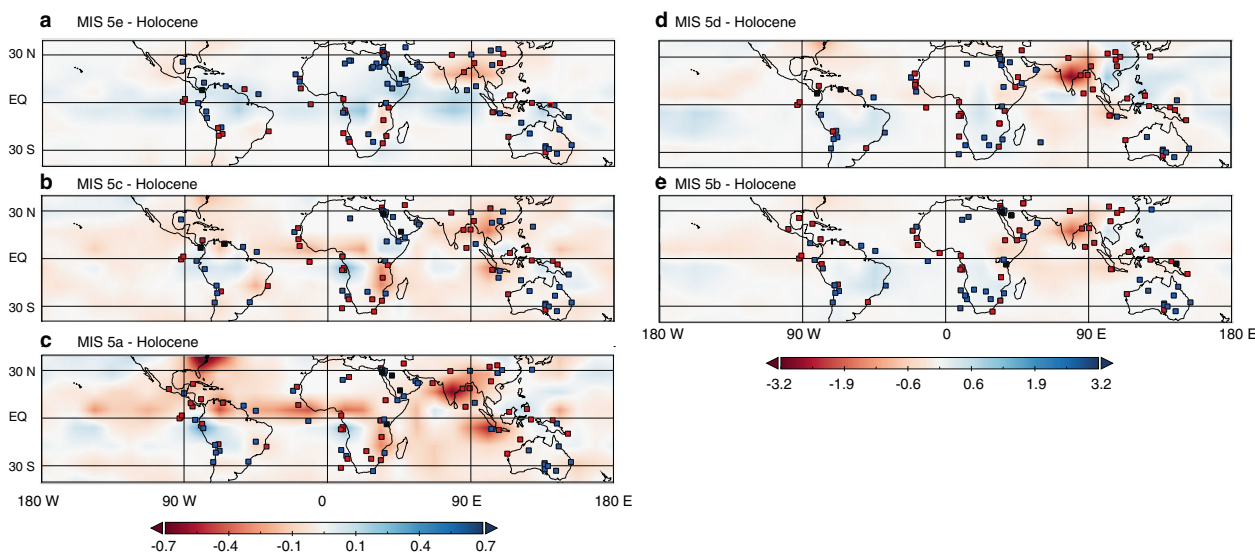


Fig. 3 MIS 5 hydroclimate reconstructions compared with the Holocene. Emulated anomaly maps of MIS 5 time slices with respect to the Holocene (12–0 ka) **a** MIS 5e—Holocene, **b** MIS 5c—Holocene, **c** MIS 5a—Holocene, **d** MIS 5d—Holocene, **e** MIS 5b—Holocene. Proxy data are superimposed; blue square = “wetter” than Holocene average, red square = “drier” than Holocene average and black square = no change (Methods and Supplementary Data 1). Emulated data are integrated from native model resolution (64 × 32 grid cells) onto 32 × 16 resolution, to smooth out grid-scale variability. Maps were produced using Panoply (source: <https://www.giss.nasa.gov/tools/panoply/>).

(Fig. 3). Across MIS 5, the western Amazon retained a consistently “wet” climate (Fig. 3). In contrast, the eastern Amazon, under the influence of the South American Monsoon, experienced drier conditions during the warmer MIS 5 sub-stages (MIS 5e, c and a) (Fig. 3a–c) and wetter, stronger monsoonal conditions during MIS 5d and b (Fig. 3d, e).

Regional precipitation gradients similarly characterize the African continent across MIS 5. Intensified rainfall in northeastern-equatorial Africa during MIS 5e contrasts with dry SE African conditions (Fig. 3a). This contrasting inter-hemispheric climatic regime during MIS 5e is thought to have provided conditions favourable for promoting human dispersal out of southern Africa northwards^{42,43}. Evidence for expansive ancient lake systems^{44,45} and cave deposits⁴⁶ in the presently arid regions of northern Africa, Arabia and the Levant (Fig. 3a) point to MIS 5e being associated with an intensified and more expanded rainfall regime in comparison to the Holocene. The penetration of monsoonal rains into northern Africa is typically impeded, associated with the high surface albedo of the Sahara Desert⁴⁷. However, the wet conditions of MIS 5e, primarily influenced by increased NHI during precession_{min}⁴⁸, would have facilitated a northward intrusion of monsoonal rain via land-surface feedbacks associated with the subsequent vegetation of the Sahara and expanded lake systems⁴⁹ (Fig. 3a). By MIS 5b (Fig. 3e), these wet conditions had largely dissipated in northeastern Africa and the Arabian Peninsula, highlighting the unique climatic window associated with the earlier half of MIS 5. The African continent was further characterized by a dipole-like precipitation pattern south of the equator, which was prevalent across all MIS 5 time slices, highlighting the competing influence of the Atlantic ITCZ to the west vs. the influence of Indian Ocean dynamics to the east^{50,51}.

In contrast to the intensified hydroclimate regime in the Levant and Arabian Peninsula during MIS 5e, both subsystems of the Asian Monsoon, the ISM and EASM, experience reduced monsoonal precipitation compared to the Holocene (Fig. 3a). This may be indicative of a lack of homogenous meridional shift of the zonal mean ITCZ or influenced by biases within the proxy signal, which remains complex within this region (Methods). The overall reduced monsoonal strength associated with MIS 5e in comparison to the Holocene over Asia (Fig. 3a) highlights discrepancies in application of the “Global Monsoon” term due to the potentially greater regional influence of land-surface feedbacks in modulating and sustaining the response of rainfall over the northeastern African tropics⁵² compared to that over the Asian domain. In addition, the differential rainfall response to warming during the Holocene and MIS 5e may highlight the competing influence of thermodynamic and dynamic responses, and the respective regional importance under warm climates controlling the loci of rainfall as is observed with the greater amount of rainfall falling over the equatorial Indian Ocean compared to the Holocene (Fig. 3a).

Concluding remarks. The integrated approach applied in this study, exploiting both multi-proxy data and model output, indicates that the spatial pattern of tropical hydroclimate in response to past climate changes cannot be explained solely by commonly ascribed mechanisms related to a meridional framework, specifically ITCZ shifts, within paleoclimate studies. Dipole-like precipitation patterns are pervasive throughout MIS 5, existing on all land masses straddling the tropics (Fig. 3), highlighting the competing influences of different ocean basins⁵³ in influencing the local internal climate dynamic response to forcing. This is further reinforced by the differing response of the regional monsoon systems, such as extreme “dry” conditions across the Indian Monsoon region, to climate warming and cooling across

MIS 5 in comparison to the Holocene, indicating the importance of competing internal and external boundary conditions in pre-conditioning monsoonal strength and loci of monsoon rainfall. Consequentially, the “Global Monsoon” term is undermined. Importantly, these regional nuances in the response of tropical hydroclimate to climate forcing has had important implications for human migration “out-of-Africa”^{42,43} and Amazonian biodiversity across MIS 5^{54,55}. The underappreciated complexity in the response of tropical rainfall to past climate forcing warrants more concentrated efforts in compiling proxy records coupled with model outputs across large spatial scales. Encouragingly, the results of this study highlight that an approximation of past hydroclimate can be discerned only when such multi-location and multi-proxy approaches are taken. A need for more concentrated proxy-model integrated studies of past warm intervals is needed considering that, regionally, hydroclimate does not respond uniformly with respect to climate forcing and thereby has important implications for future predictions of tropical rainfall patterns in response to climate change.

Methods

Records generated from this study. Site U1446, northern Bay of Bengal ($19^{\circ} 5.02'N$, $85^{\circ} 44'E$, water depth 1430 m), and U1448, Andaman Sea ($10^{\circ} 38.03'N$, $93^{\circ} 00'E$, water depth 1098 m), were drilled during International Ocean Discovery Program (IODP) Expedition 353 to the Bay of Bengal.

Around 6–50 individuals of the planktic foraminifera *Globigerinoides ruber* *sensu stricto* were picked from the 250–355 μ m size fraction, cracked open with a needle and split into two fractions prior to geochemical cleaning and analysis. Planktic foraminifera $\delta^{18}\text{O}$ analyses were performed at the British Geological Survey, NERC Isotope Geosciences Facilities, Keyworth, using an Isoprime dual inlet mass spectrometer with multiprep device. The reproducibility of $\delta^{18}\text{O}$ $\pm 0.05\text{‰}$ (1σ) was based on replicate measurements of carbonate standards. All data are reported on the Vienna Pee Dee Belemnite scale.

Details of the procedure for cleaning prior to trace-element analysis and subsequent derivation of temperature (SST) and seawater $\delta^{18}\text{O}$ ($\delta^{18}\text{O}_{\text{sw-IVC}}$) have been described in ref. ²⁴; the same approaches are applied here. Samples from Sites U1446 and U1448 were subjected to a full trace-element cleaning method⁵⁶ with slight modifications, namely an extended clay-removal step was performed to ensure removal of fine clays, which might bias Mg/Ca results⁵⁷. Samples were analysed at the Open University using an Agilent Technologies Triple-Quad Inductively Coupled Plasma-Mass Spectrometer 8800. Samples from Site U1446 and Site U1448 were run at 10 and 25 p.p.m. Ca, respectively. Reproducibility of a synthetic monitor standard of Mg/Ca ratio of 3.33 mmol/mol was 0.06 mmol/mol during the analytical window. Following ref. ⁵⁸, elements were normalized to Ca and ratios were calculated using calibration derived from matrix-matched standards with varying trace-element concentrations. Contaminant ratios (Al/Ca and Fe/Ca) were monitored to assess any contamination by clays and organic material. Samples that returned values of Al/Ca > 300 $\mu\text{mol/mol}$ were discarded; in total, 20 *G. ruber* ss samples with high Al/Ca values, including two samples with anomalously low Mg/Ca ratios from Site U1446, were rejected. Linear interpolation between data points was applied to provide a first-order estimation of missing Mg/Ca (SST) values. It is inferred that this is sufficient for deriving the local $\delta^{18}\text{O}_{\text{sw-IVC}}$ due to U1446 *G. ruber* ss $\delta^{18}\text{O}_{\text{C}}$ being overwhelmed by the effects of the local hydrology (precipitation and runoff) as exhibited by the significant magnitudes of change throughout MIS 5 ranging up to 2.5‰ (Supplementary Fig. 6). Furthermore, annual temperature changes within the modern-day Bay of Bengal are limited by a couple of degrees⁵⁹ and, therefore, the estimated Mg/Ca values should be within error. SST was estimated using the widely applied multi-species equation from the North Atlantic⁶⁰ with a correction for a 10% reduction in Mg/Ca following ref. ⁶¹, associated with the reductive method; $\text{Mg/Ca} = 0.342(\pm 0.02)\exp(0.09(\pm 0.03) \times T)$. To isolate the local $\delta^{18}\text{O}_{\text{sw}}$, both a temperature and an ice volume correction was applied to the calcite $\delta^{18}\text{O}$; $T^{\circ}\text{C} = 14.9(\pm 0.1) - 4.8(\pm 0.08) \times (\delta^{18}\text{O}_{\text{C}} - (\delta^{18}\text{O}_{\text{sw}} - 0.27))$ ⁶². A sea-level correction was applied by exploiting the benthic $\delta^{18}\text{O}$ of both U1446 and U1448, which were scaled to the Waelbroeck sea-level curve⁶³.

Compilation of low-latitude hydroclimate proxy records. A selection of existing paleoclimate records that cover a latitudinal band of $\sim 30^{\circ}\text{N}$ to 30°S , extending wholly or partially across MIS 5 (~ 130 –74 ka) and have been inferred to capture past changes in hydroclimate, were compiled (Supplementary Data 1).

Paleoclimate records, which had a resolution of 2 ka or better, with publicly archived data, were gathered to perform the time-series comparisons (Supplementary Data 1). Application of this criteria resulted in a remaining database of 55 hydroclimate records, including the 2 new records generated in this study (Supplementary Fig. 1). All records were normalized and linear interpolation was performed to resample datasets onto a common age scale at a 1 ka resolution

(i.e., the same resolution as the model time series). Records were subsequently assigned “Regions”, to compare with the regional time series of the emulation of precipitation. Largely, these followed the latitude-longitude of the proxy site location, which denoted the corresponding region (Fig. 1). However, records within the IPWP^{35,36} and northeast South American margin⁶⁴ were assigned to Regions 6 and 4 rather than Regions 3 and 2, respectively.

Further, we apply a qualitative approach^{19,31,65} to compare regional precipitation variability with model derived anomaly maps (MIS 5 time-slice average—Holocene (12–0 ka average signal)), where values 1 (wetter than Holocene, blue), 0 (no change, black) and −1 (drier than Holocene, red) were assigned to paleoclimate records based on the original interpretation and/or assessment with the average Holocene (12–0 ka) values where available (Supplementary Data 1). This strategy was followed due to the complex nature of proxies applied to reconstruct past hydroclimate (Methods, see “Reconstructing past hydroclimate”) and consequent limitations in producing and comparing any meaningful quantitative estimates (e.g., rainfall (mm)) unlike studies that synthesize past SST changes (°C)¹⁶. We believe the time-slice strategy applied (i.e., average signal across the interstadials (MIS 5a, c and e) and stadial (MIS 5b, d) periods compared to the average Holocene) permits a representative qualification of the proxy signal with chronological and proxy errors suppressed compared to studies that employ a single time-point approach (e.g., see ref. ¹⁹).

Age model. The age model and tuning strategy of Site U1446 has been initially described in Nilsson-Kerr et al.²⁴ and has subsequently undergone further refinement for this study. U1446 benthic foraminifera (*Cibicidoides wuellerstorfi* and *Uvigerina spp.*) oxygen isotope ($\delta^{18}\text{O}$) (S. C. Clemens, unpublished) was similarly transferred onto the Antarctic Ice Core Chronology (AICC2012)^{66,67} (Supplementary Fig. 7).

To reduce potential offsets induced by differing tuning strategies, a common age model was applied, where possible, to all marine records that were extracted for time-series analysis. U1446 benthic $\delta^{18}\text{O}$ was used as a reference target for benthic $\delta^{18}\text{O}$ records to transfer onto AICC2012 chronology. Benthic $\delta^{18}\text{O}$ of sediment cores GeoB7920-2⁶⁸, GeoB9528-3⁶⁹, RC09-166⁴³, MD06-3075³⁶, MD96-2048⁷⁰, GeoB3375-1⁷¹, TR163-1972, TR163-22⁷³, ODP 659 and ODP 658⁷⁴, ODP 1146⁷⁵, IODP Site U1429³² and M125-55-7/8⁷⁶ were all graphically correlated to U1446 benthic $\delta^{18}\text{O}$ using Analyseries⁷⁷ (Supplementary Fig. 8). Linear interpolation was subsequently applied between tie-points to construct the new-age models.

Cores GeoB7925-1, GeoB1028-5, GeoB1016-3, GeoB1008-3, GeoB4901-8, GeoB9516-5⁷⁸ and MD08-3167^{64,79} did not undergo age-model refinement, as these were on AICC2012 chronology already. The Ti content of cores GeoB9506-1 and GeoB9527-5³⁹ were transferred onto AICC2012 chronology via graphical correlation to the Ti content of nearby core GeoB9516-5^{39,78} (Supplementary Fig. 9). Graphical alignment of planktic $\delta^{18}\text{O}$ was applied for cores that lacked corresponding benthic $\delta^{18}\text{O}$ data. ODP 108-658 planktic $\delta^{18}\text{O}$ was used as a reference target for cores MD203-2707⁸⁰, ODP 999 A⁸¹, MD05-2925⁸², GeoB3911-183⁸³, MD00-2361⁸⁴, MD96-2094⁸⁵ and KX-12-1⁸⁶ (Supplementary Fig. 10).

The original chronologies of Cores MD98-2152⁸⁷, GeoTu_SL110⁸⁸, MD03-261 and SO130-289KL⁵ were retained due to lack of available planktic or benthic $\delta^{18}\text{O}$. The original chronology of Core MD02-2529⁸⁹ and ODP 967⁹⁰ was also kept.

Precipitation emulation. Emulated precipitation fields were derived using PaleoPGEM²¹. The approach applies Gaussian process emulation of the singular value decomposition of ensembles of runs from the intermediate-complexity atmosphere–ocean GCM PLASIM-GENIE²² with varied boundary-condition forcing (CO₂, orbit and ice volume). The underlying simulations were performed at spectral T21 and atmospheric resolution (5.625°) with 10 vertical layers, and a matching ocean grid with 16 logarithmically spaced depth levels, using the optimized parameter set²¹. Spatial fields of annual average precipitation were then emulated at 1000-year intervals, driven by the time series of scalar boundary-condition forcing, and assuming the climate is in quasi-equilibrium. Twenty Gaussian process emulators were built and applied, and the mean is presented in Figs. 2 and 3. In Fig. 3, emulated data are integrated from the native model resolution (64 × 32 grid cells; Supplementary Fig. 11) onto 32 × 16 resolution, to smooth out the grid-scale structure. The spatial distribution and magnitude of PaleoPGEM climate and corresponding uncertainties have been shown to be comparable to model inter-comparisons (Section 9 of ref. ²¹) in state-of-the-art climate models as measured by spatial fields of mean and variance across ensembles of the Paleoclimate Modelling Intercomparison Project (PMIP) simulations of the Last Glacial Maximum and Mid Holocene²¹, noting that PaleoPGEM uncertainties derive from the emulation step of the reconstructions, and thus underestimate the full simulation uncertainty. Supplementary Fig. 12b compares the PaleoPGEM precipitation anomaly between 127 ka and Preindustrial with the results from the *lig12k* simulation for CMIP6-PMIP4 (Supplementary Fig. 12a). Considering the intermediate resolution of PaleoPGEM, there are discernible similarities in the large-scale precipitation anomalies reconstructed with the multi-model ensemble average (Supplementary Fig 12a). Furthermore, the PLASIM-GENIE simulation of present day precipitation shares similar large-scale spatial patterns with that of measured precipitation (Fig. 1 and Supplementary Fig. 13). Our compilation of the available proxy data in time-series format for low-latitude hydroclimate (30°N–30°S) (Supplementary Fig. 1d) and for both northern

hemisphere low latitudes (0–30°N) (Supplementary Fig. 1f) and southern hemisphere low latitudes (0–30°S) (Supplementary Fig. 1h), as well as the time-varying PaleoPGEM emulations, correspond well with the CCSM3 model output for terrestrial rainfall (Supplementary Fig. 1c, e, g) and to the record of the ΔDE^* (Supplementary Fig. 1a,i), inferred as a measure of the large-scale low-latitude hydroclimate signal²³.

Reconstructing past hydroclimate. Sea-level changes altering the transport of riverine material to the ocean can bias applications of grain size, clay mineral content and elemental concentrations of marine sediment cores, inferred to track riverine runoff and continental weathering, as a result of changes in continental precipitation intensity^{91,92}. Furthermore, normalization of X-Ray Fluorescence-derived element concentrations to calcium (e.g., Fe/Ca and Ti/Ca), widespread within the paleoclimate studies (and hence, several examples can be found in Supplementary Data 1), may be biased by the effect of biogenic dilution⁹³, whereas proxies inferred to trace past vegetation changes (e.g., pollen assemblage and plant leaf waxes) in response to changes in rainfall regime are similarly influenced by changes in coastal environments^{94,95}. Inferences of past vegetation as representing hydroclimate may further be obscured by an increasing amount of anthropogenic activities occurring during the Holocene (e.g., anthropogenic fire and burning). Isotopic tracers ($\delta^{18}\text{O}$, δD) of past rainfall hosted in carbonates (e.g., speleothems and microfossils (foraminifera) or plant leaf waxes are commonly applied to capture changes in past rainfall intensity (e.g., see refs. ^{69,96,97}). However, the isotopic composition of precipitation received at a site is fundamentally determined by several processes including (but not limited to) evaporation (evapotranspiration), moisture transport and the associated amalgamation of differing moisture sources^{3,98–101}. The isotopic signal is further determined by a mixture of local processes inherent to the proxy archive. The isotopic composition of leaf wax can be complicated by different plant types^{102,103}, whereas speleothem $\delta^{18}\text{O}$ can be influenced by cave temperature, soil and karstic processes^{104,105}. Residuals of foraminifera $\delta^{18}\text{O}$ (seawater $\delta^{18}\text{O}$) (having corrected for the effects of temperature and sea level, which carry their own respective uncertainties^{106–109}) commonly used as a means of capturing changes in surface freshening in marginal locations involve large uncertainties if a conversion to salinity is applied¹¹⁰ and any freshening by rainfall alone is expected to lack any discernible signal. Modern empirical studies^{104,111,112}, application of isotope-enabled models^{99,101,113} and refined calibration approaches^{114,115} have been employed, to disentangle the varying complications to permit confidence in paleoclimate reconstructions, but with limited success.

In addition to the difficulties associated with the acquisition of an authentic record of past rainfall variability, each proxy record is further hampered by the time-averaging of sediments and associated chronological uncertainties. The time-slice approach taken in this study associated with investigation of past hydroclimate patterns across MIS 5 compared to the Holocene (Fig. 3) alleviates some chronological biases due to averaging of several thousands of years (e.g., MIS 5e, 130–115 ka). Thereby, ensuring a representative signal from that time slice has been acquired unlike single time-point approaches. However, the time-series approach to regional hydroclimate reconstruction (Fig. 1) will suffer discrepancies associated with chronological errors, although these have been minimized by ensuring marine records are all placed on a consistent chronology. Chronological errors exert a large influence on paleoclimate proxy records and, thus, our ability to constrain timing/phasing will always be limited to an extent. This is further impacted by the proxy amalgamating a system-wide response to climate forcing (e.g., river runoff and sea-level changes).

Considering the aforementioned factors, it is promising that the average combined proxy signal (i.e., the combined average of all the proxy record z-scores from each respective region) approximates past hydroclimate as that estimated by the emulation for the different regions (Fig. 2). This underlines the importance of multi-proxy, basin-wide strategies, to circumvent locally inflicted biases, both climatically and carrier induced, when inferring past hydroclimate.

Holocene vs. MIS 5e. MIS 5e has largely been regarded as representing one of the warmer interglacials of the Late Pleistocene experiencing similar CO₂ levels to P11¹⁶ (Supplementary Fig. 14d) with sea level 6–9 m higher than present¹¹⁷. Primarily, it was in the high latitudes of the Northern Hemisphere where anomalous warming with reconstructed temperatures was witnessed, suggesting >5 °C warmer than P11¹⁸, whereas the low latitudes remained similar to the present-day SSTs¹⁶. The climatic conditions of MIS 5e are mainly a result of preconditioning by a combination of high eccentricity (Supplementary Fig. 14b,i) enhancing the effects of precession_{min} (Supplementary Fig. 14b,ii)¹¹⁹. This orbital configuration resulted in enhanced seasonality (stronger insolation received during Northern Hemisphere summers) compared to the Holocene but the overall mean annual insolation was lower¹²⁰. Obliquity maximum was reached prior to MIS 5e at ~131 ka (Supplementary Fig. 14 a). Meanwhile, precession peaked at ~127 ka prior to its decline by ~117 ka (Supplementary Fig. 14b,ii). Across MIS 5e, the orbital configuration varied (Supplementary Fig. 14); therefore, latitudinal temperature gradients and seasonality were not stationary throughout this interval, and subsequently would have been accompanied by variations in the tropical hydroclimate. The averaged time-slice approach taken, i.e., MIS 5e 130–116 ka and Holocene 12–0 ka, encompasses both the increase into and attainment of peak interglacial conditions,

as well as the descent from peak interglacial conditions and, thus, ideally represent the average tropical hydroclimate response under a generally warm climatic state.

Data availability

Proxy data generated in this study (U1446 and U1448) and regional time-series precipitation emulation data can be found archived at <https://doi.org/10.1594/PANGAEA.920668>. All proxy data used in the analysis are publicly available and detailed information can be found in Supplementary Data 1.

Received: 28 October 2020; Accepted: 22 February 2021;

Published online: 19 March 2021

References

- Allen, M. R. & Ingram, W. J. Constraints on future changes in climate and the hydrologic cycle. *Nature* **419**, 228–232 (2002).
- Huang, P., Xie, S.-P., Hu, K., Huang, G. & Huang, R. Patterns of the seasonal response of tropical rainfall to global warming. *Nat. Geosci.* **6**, 357–361 (2013).
- Konecky, B. L., Noone, D. C. & Cobb, K. M. The influence of competing hydroclimatic processes on stable isotope ratios in tropical rainfall. *Geophys. Res. Lett.* **46**, 1622–1633 (2019).
- Strikis, N. M. et al. South American monsoon response to iceberg discharge in the North Atlantic. *Proc. Natl Acad. Sci. USA* **115**, 3788–3793 (2018).
- Deplazes, G. et al. Links between tropical rainfall and North Atlantic climate during the last glacial period. *Nat. Geosci.* **6**, 213–217 (2013).
- Arbuszewski, J. A., deMenocal, P. B., Cléroux, C., Bradtmiller, L. & Mix, A. Meridional shifts of the Atlantic intertropical convergence zone since the Last Glacial Maximum. *Nat. Geosci.* **6**, 959–962 (2013).
- Wang, X. et al. Wet periods in northeastern Brazil over the past 210 kyr linked to distant climate anomalies. *Nature* **432**, 740–743 (2004).
- Bischoff, T. & Schneider, T. The equatorial energy balance, ITCZ position, and double-ITCZ bifurcations. *J. Clim.* **29**, 2997–3013 (2016).
- Roberts, W. H. G., Valdes, P. J. & Singarayer, J. S. Can energy fluxes be used to interpret glacial/interglacial precipitation changes in the tropics? *Geophys. Res. Lett.* **44**, 6373–6382 (2017).
- Singarayer, J. S., Valdes, P. J. & Roberts, W. H. G. Ocean dominated expansion and contraction of the late Quaternary tropical rainbelt. *Sci. Rep.* **7**, 9382 (2017).
- McGee, D., Donohoe, A., Marshall, J. & Ferreira, D. Changes in ITCZ location and cross-equatorial heat transport at the Last Glacial Maximum, Heinrich Stadial 1, and the mid-Holocene. *Earth Planet. Sci. Lett.* **390**, 69–79 (2014).
- Scroxton, N. et al. Hemispherically in-phase precipitation variability over the last 1700 years in a Madagascar speleothem record. *Quat. Sci. Rev.* **164**, 25–36 (2017).
- Yan, H. et al. Dynamics of the intertropical convergence zone over the western Pacific during the Little Ice Age. *Nat. Geosci.* **8**, 315–320 (2015).
- Trenberth, K. E. et al. The global monsoon as seen through the divergent atmospheric circulation. *J. Clim.* **13**, 3969–3993 (2000).
- Caley, T. et al. Orbital timing of the Indian, East Asian and African boreal monsoons and the concept of a ‘global monsoon’. *Quat. Sci. Rev.* **30**, 3705–3715 (2011).
- Hoffman, J. S., Clark, P. U., Parnell, A. C. & He, F. Regional and global sea-surface temperatures during the last interglaciation. *Science* **355**, 276–279 (2017).
- Kaufman, D. et al. A global database of Holocene paleotemperature records. *Sci. Data* **7**, 115 (2020).
- Tierney, J. E. et al. Glacial cooling and climate sensitivity revisited. *Nature* **584**, 569–573 (2020).
- Scussolini, P. et al. Agreement between reconstructed and modeled boreal precipitation of the Last Interglacial. *Sci. Adv.* **5**, eaax7047 (2019).
- Konecky, B. L. et al. The Iso2k database: a global compilation of paleo- $\delta^{18}\text{O}$ and $\delta^{2\text{H}}$ records to aid understanding of Common Era climate. *Earth Syst. Sci. Data* **12**, 2261–2288 (2020).
- Holden, P. B. et al. PALEO-PGEM v1.0: a statistical emulator of Pliocene–Pleistocene climate. *Geosci. Model Dev.* **12**, 5137–5155 (2019).
- Holden, P. B. et al. Climate–carbon cycle uncertainties and the Paris Agreement. *Nat. Clim. Chang.* **8**, 609–613 (2018).
- Huang, E. et al. Dole effect as a measurement of the low-latitude hydrological cycle over the past 800 ka. *Sci. Adv.* **6**, eaba4823 (2020).
- Nilsson-Kerr, K. et al. Role of Asian summer monsoon subsystems in the inter-hemispheric progression of deglaciation. *Nat. Geosci.* **12**, 290–295 (2019).
- Clemens, S. C. & Prell, W. L. A 350,000 year summer-monsoon multi-proxy stack from the Owen Ridge, Northern Arabian Sea. *Mar. Geol.* **201**, 35–51 (2003).
- Gebregiorgis, D. et al. Southern Hemisphere forcing of South Asian monsoon precipitation over the past ~1 million years. *Nat. Commun.* **9**, 4702 (2018).
- Maher, B. A. & Thompson, R. Oxygen isotopes from Chinese caves: records not of monsoon rainfall but of circulation regime. *J. Quat. Sci.* **27**, 615–624 (2012).
- Liu, X., Liu, Z., Kutzbach, J. E., Clemens, S. C. & Prell, W. L. Hemispheric insolation forcing of the Indian Ocean and Asian monsoon: local versus remote impacts. *J. Clim.* **19**, 6195–6208 (2006).
- Prell, W. L. & Kutzbach, J. E. Sensitivity of the Indian monsoon to forcing parameters and implications for its evolution. *Nature* **360**, 647–652 (1992).
- Cheng, H. et al. The Asian monsoon over the past 640,000 years and ice age terminations. *Nature* **534**, 640–646 (2016).
- DiNizio, P. N. & Tierney, J. E. The effect of sea level on glacial Indo-Pacific climate. *Nat. Geosci.* **6**, 485–491 (2013).
- Clemens, S. C. et al. Precession-band variance missing from East Asian monsoon runoff. *Nat. Commun.* **9**, 3364 (2018).
- Deplazes, G. et al. Weakening and strengthening of the Indian monsoon during Heinrich events and Dansgaard-Oeschger oscillations. *Paleoceanography* **29**, 99–114 (2014).
- Beck, J. W. et al. A 550,000-year record of East Asian monsoon rainfall from ^{10}Be in loess. *Science* **360**, 877–881 (2018).
- Carolin, S. A. et al. Northern Borneo stalagmite records reveal West Pacific hydroclimate across MIS 5 and 6. *Earth Planet. Sci. Lett.* **439**, 182–193 (2016).
- Fraser, N., Kuhnt, W., Holbourn, A., Bolliet, T. & Andersen, N. Precipitation variability within the West Pacific Warm Pool over the past 120 ka: evidence from offshore southern Mindanao, Philippines. *Paleoceanography* **16**, 1094–1110 (2014).
- Tachikawa, K. et al. The precession phase of hydrological variability in the Western Pacific Warm Pool during the past 400 ka. *Quat. Sci. Rev.* **30**, 3716–3727 (2011).
- Konecky, B. L. et al. Atmospheric circulation patterns during late Pleistocene climate changes at Lake Malawi, Africa. *Earth Planet. Sci. Lett.* **312**, 318–326 (2011).
- Itambi, A. C., von Dobeneck, T., Mulitza, S., Bickert, T. & Heslop, D. Millennial-scale northwest African droughts related to Heinrich events and Dansgaard-Oeschger cycles: Evidence in marine sediments from offshore Senegal. *Paleoceanography* **24**, PA1205 (2009).
- Daniau, A.-L. et al. Orbital-scale climate forcing of grassland burning in southern Africa. *Proc. Natl Acad. Sci. USA* **110**, 5069–5073 (2013).
- Denniston, R. F. et al. Expansion and contraction of the Indo-Pacific tropical rain belt over the last three millennia. *Sci. Rep.* **6**, 34485 (2016).
- Timmermann, A. & Friedrich, T. Late Pleistocene climate drivers of early human migration. *Nature* **538**, 92–95 (2016).
- Tierney, J. E., deMenocal, P. B. & Zander, P. D. A climatic context for the out-of-Africa migration. *Geology* **45**, 1023–1026 (2017).
- Larrasaña, J. C., Roberts, A. P. & Rohling, E. J. Dynamics of Green Sahara Periods and their role in Hominin Evolution. *PLoS One* **8**, e76514 (2013).
- Drake, N. A. et al. Reconstructing palaeoclimate and hydrological fluctuations in the Fezzan Basin (southern Libya) since 130 ka: a catchment-based approach. *Quat. Sci. Rev.* **200**, 376–394 (2018).
- Nicholson, S. L. et al. Pluvial periods in Southern Arabia over the last 1.1 million-years. *Quat. Sci. Rev.* **229**, 106112 (2020).
- Street-Perrott, F. A., Mitchell, J. F. B., Marchand, D. S. & Brunner, J. S. Milankovitch and albedo forcing of the tropical monsoons: a comparison of geological evidence and numerical simulations for 9000 yBP. *Trans. R. Soc. Edinb. Earth Sci.* **81**, 407–427 (1990).
- Kutzbach, J. E. et al. African climate response to orbital and glacial forcing in 140,000-y simulation with implications for early modern human environments. *Proc. Natl Acad. Sci. USA* **117**, 2255–2264 (2020).
- Broström, A. et al. Land surface feedbacks and palaeomonsoons in northern Africa. *Geophys. Res. Lett.* **25**, 3615–3618 (1998).
- Tierney, J. E., Russell, J. M., Sinnenberg Damsté, J. S., Huang, Y. & Verschuren, D. Late Quaternary behavior of the East African monsoon and the importance of the Congo Air Boundary. *Quat. Sci. Rev.* **30**, 798–807 (2011).
- Singarayer, J. S. & Burrough, S. L. Interhemispheric dynamics of the African rainbelt during the late Quaternary. *Quat. Sci. Rev.* **124**, 48–67 (2015).
- Schurges, G. et al. The effect of land surface changes on Eemian climate. *Clim. Dyn.* **29**, 357–373 (2007).
- Tierney, J. E. et al. Northern Hemisphere controls on tropical Southeast African climate during the past 60,000 years. *Science* **322**, 252–255 (2008).
- Cheng, H. et al. Climate change patterns in Amazonia and biodiversity. *Nat. Commun.* **4**, 1411 (2013).
- Silva, S. M. et al. A dynamic continental moisture gradient drove Amazonian bird diversification. *Sci. Adv.* **5**, eaat5752 (2019).
- Boyle, E. A. & Keigwin, L. D. Comparison of Atlantic and Pacific paleochemical records for the last 215,000 years: changes in deep ocean circulation and chemical inventories. *Earth Planet. Sci. Lett.* **76**, 135–150 (1985).

57. Barker, S., Greaves, M. & Elderfield, H. A study of cleaning procedures used for foraminiferal Mg/Ca paleothermometry. *Geochemistry. Geophys. Geosyst.* **4**, 8407 (2003).

58. Rosenthal, Y., Field, P. M., Sherrell, R. M. & Sherrell, R. M. Precise determination of element/calcium ratios in calcareous samples using sector field inductively coupled plasma mass spectrometry. *Anal. Chem.* **71**, 3248–3253 (1999).

59. Boyer, T. P. *et al.* *World Ocean Database 2013*. (NOAA, 2013).

60. Anand, P., Elderfield, H. & Conte, M. H. Calibration of Mg/Ca thermometry in planktonic foraminifera from a sediment trap time series. *Paleoceanography* **18**, 1050 (2003).

61. Gibbons, F. T. *et al.* Deglacial $\delta^{18}\text{O}$ and hydrologic variability in the tropical Pacific and Indian Oceans. *Earth Planet. Sci. Lett.* **387**, 240–251 (2014).

62. Bemis, B. E., Spero, H. J., Bijma, J. & Lea, D. W. Reevaluation of the oxygen isotopic composition of planktonic foraminifera: experimental results and revised paleotemperature equations. *Paleoceanography* **13**, 150–160 (1998).

63. Waelbroeck, C. *et al.* Sea-level and deep water temperature changes derived from benthic foraminifera isotopic records. *Quat. Sci. Rev.* **21**, 295–305 (2002).

64. Govin, A. *et al.* Terrigenous input off northern South America driven by changes in Amazonian climate and the North Brazil Current retroflection during the last 250 ka. *Clim. Past* **10**, 843–862 (2014).

65. DiNezio, P. N. *et al.* Glacial changes in tropical climate amplified by the Indian Ocean. *Sci. Adv.* **4**, eaat9658 (2018).

66. Bazin, L. *et al.* An optimized multi-proxy, multi-site Antarctic ice and gas orbital chronology (AICC2012): 120–800 ka. *Clim. Past* **9**, 1715–1731 (2013).

67. Veres, D. *et al.* The Antarctic ice core chronology (AICC2012): an optimized multi-parameter and multi-site dating approach for the last 120 thousand years. *Clim. Past* **9**, 1733–1748 (2013).

68. Tjallingii, R., Stattegger, K., Wetzel, A. & Van Phach, P. Infilling and flooding of the Mekong River incised valley during deglacial sea-level rise. *Quat. Sci. Rev.* **29**, 1432–1444 (2010).

69. Castañeda, I. S. *et al.* Wet phases in the Sahara/Sahel region and human migration patterns in North Africa. *Proc. Natl Acad. Sci. USA* **106**, 20159–20163 (2009).

70. Caley, T. *et al.* A two-million-year-long hydroclimatic context for hominin evolution in southeastern Africa. *Nature* **560**, 76–79 (2018).

71. Lamy, F. *et al.* Precession modulation of the South Pacific westerly wind belt over the past million years. *Proc. Natl Acad. Sci. USA* **116**, 23455–23460 (2019).

72. Lea, D. W. *et al.* Paleoclimate history of Galápagos surface waters over the last 135,000 yr. *Quat. Sci. Rev.* **25**, 1152–1167 (2006).

73. Lea, D. W., Pak, D. K. & Spero, H. J. Climate impact of late quaternary equatorial Pacific sea surface temperature variations. *Science* **289**, 1719–1724 (2000).

74. Sarnthein, M. & Tiedemann, R. Toward a high-resolution stable isotope stratigraphy of the last 3.4 million years: sites 658 and 659 off Northwest Africa. In *Proc. Ocean Drilling Program, 108 Scientific Results*, <https://doi.org/10.2973/odp.proc.sr.108.159.1989> (Ocean Drilling Program, 1989).

75. Caballero-Gill, R. P., Clemens, S. C. & Prell, W. L. Direct correlation of Chinese speleothem $\delta^{18}\text{O}$ and South China Sea planktonic $\delta^{18}\text{O}$: transferring a speleothem chronology to the benthic marine chronology. *Paleoceanography* **27**, PA2203 (2012).

76. Hou, A. *et al.* Forcing of western tropical South Atlantic sea surface temperature across three glacial-interglacial cycles. *Glob. Planet. Change* **188**, 103150 (2020).

77. Paillard, D., Labeyrie, L. & Yiou, P. Macintosh Program performs time-series analysis. *Eos (Washington, DC)* **379**, 77 (1996).

78. Govin, A., Varma, V. & Prange, M. Astronomically forced variations in western African rainfall (21°N–20°S) during the Last Interglacial period. *Geophys. Res. Lett.* **41**, 2117–2125 (2014).

79. Collins, J. A., Schefuß, E., Govin, A., Multizzi, S. & Tiedemann, R. Insolation and glacial-interglacial control on southwestern African hydroclimate over the past 140 000 years. *Earth Planet. Sci. Lett.* **398**, 1–10 (2014).

80. Weldeab, S., Lea, D. W., Schneider, R. R. & Andersen, N. 155,000 years of West African monsoon and ocean thermal evolution. *Science* **316**, 1303–1307 (2007).

81. Schmidt, M. W., Spero, H. J. & Lea, D. W. Links between salinity variation in the Caribbean and North Atlantic thermohaline circulation. *Nature* **428**, 160–163 (2004).

82. Lo, L. *et al.* Nonlinear climatic sensitivity to greenhouse gases over past 4 glacial-interglacial cycles. *Sci. Rep.* **7**, 4626 (2017).

83. Dupont, L. M. & Kuhlmann, H. Glacial-interglacial vegetation change in the Zambezi catchment. *Quat. Sci. Rev.* **155**, 127–135 (2017).

84. Stuut, J. B. W., Temmelsfeld, F. & De Deckker, P. A 550ka record of aeolian activity near north west cape, australia: Inferences from grain-size distributions and bulk chemistry of SE indian ocean deep-sea sediments. *Quat. Sci. Rev.* **83**, 83–94 (2014).

85. Stuut, J.-B. W. *et al.* A 300-kyr record of aridity and wind strength in southwestern Africa: inferences from grain-size distributions of sediments on Walvis Ridge, SE Atlantic. *Mar. Geol.* **180**, 221–233 (2002).

86. Dang, H. *et al.* Orbital and sea-level changes regulate the iron-associated sediment supplies from Papua New Guinea to the equatorial Pacific. *Quat. Sci. Rev.* **239**, 106361 (2020).

87. Windler, G., Tierney, J. E., DiNezio, P. N., Gibson, K. & Thunell, R. Shelf exposure influence on Indo-Pacific Warm Pool climate for the last 450,000 years. *Earth Planet. Sci. Lett.* **516**, 66–76 (2019).

88. Ehrmann, W., Schmidl, G., Seidel, M., Krüger, S. & Schulz, H. A distal 140 kyr sediment record of Nile discharge and East African monsoon variability. *Clim. Past* **12**, 713–727 (2016).

89. Leduc, G. *et al.* Moisture transport across Central America as a positive feedback on abrupt climatic changes. *Nature* **445**, 908–911 (2007).

90. Grant, K. M. *et al.* A 3 million year index for North African humidity/aridity and the implication of potential pan-African Humid periods. *Quat. Sci. Rev.* **171**, 100–118 (2017).

91. Aiello, I. W. *et al.* Climate, sea level and tectonic controls on sediment discharge from the Sepik River, Papua New Guinea during the Mid- to Late Pleistocene. *Mar. Geol.* **415**, 105954 (2019).

92. Gebregiorgis, D. *et al.* What can we learn from X-ray fluorescence core scanning data? A Paleomonsoon Case Study. *Geochemistry, Geophys. Geosystems* **21**, e2019GC008414 (2020).

93. Govin, A. *et al.* Distribution of major elements in Atlantic surface sediments (36°N–49°S): Imprint of terrigenous input and continental weathering. *Geochem. Geophys. Geosyst.* **13**, Q01013 (2012).

94. Chen, Y. *et al.* Wetland expansion on the continental shelf of the northern South China Sea during deglacial sea level rise. *Quat. Sci. Rev.* **231**, 106202 (2020).

95. French, K. L. *et al.* Millennial soil retention of terrestrial organic matter deposited in the Bengal Fan. *Sci. Rep.* **8**, 11997 (2018).

96. Wang, Y. *et al.* Millennial- and orbital-scale changes in the East Asian monsoon over the past 224,000 years. *Nature* **451**, 1090–1093 (2008).

97. Cheng, H. *et al.* A penultimate glacial monsoon record from Hulu Cave and two-phase glacial terminations. *Geology* **34**, 217–220 (2006).

98. Pausata, F. S. R., Battisti, D. S., Nisancioglu, K. H. & Bitz, C. M. Chinese stalagmite $\delta^{18}\text{O}$ controlled by changes in the Indian monsoon during a simulated Heinrich event. *Nat. Geosci.* **4**, 474–480 (2011).

99. Caley, T., Roche, D. M. & Renssen, H. Orbital Asian summer monsoon dynamics revealed using an isotope-enabled global climate model. *Nat. Commun.* **5**, 5371 (2014).

100. Battisti, D. S., Ding, Q. & Roe, G. H. Coherent pan-Asian climatic and isotopic response to orbital forcing of tropical insolation. *J. Geophys. Res. Atmos.* **119**, 11997–12020 (2014).

101. Tabor, C. R. *et al.* Interpreting precession-driven $\delta^{18}\text{O}$ variability in the South Asian monsoon region. *J. Geophys. Res. Atmos.* **123**, 5927–5946 (2018).

102. Wang, Y. V. *et al.* What does leaf wax δD from a mixed C3/C4 vegetation region tell us? *Geochim. Cosmochim. Acta* **111**, 128–139 (2013).

103. Hou, J., D’Andrea, W. J. & Huang, Y. Can sedimentary leaf waxes record D/H ratios of continental precipitation? Field, model, and experimental assessments. *Geochim. Cosmochim. Acta* **72**, 3503–3517 (2008).

104. Lachniet, M. S. Climatic and environmental controls on speleothem oxygen-isotope values. *Quat. Sci. Rev.* **28**, 412–432 (2009).

105. Baker, A. *et al.* Global analysis reveals climatic controls on the oxygen isotope composition of cave drip water. *Nat. Commun.* **10**, 2984 (2019).

106. Gray, W. R. *et al.* The effects of temperature, salinity, and the carbonate system on Mg/Ca in Globigerinoides ruber (white): a global sediment trap calibration. *Earth Planet. Sci. Lett.* **482**, 607–620 (2017).

107. Kopp, R. E., Simons, F. J., Mitrovica, J. X., Maloof, A. C. & Oppenheimer, M. Probabilistic assessment of sea level during the last interglacial stage. *Nature* **462**, 863–867 (2009).

108. Dutton, A. *et al.* Sea-level rise due to polar ice-sheet mass loss during past warm periods. *Science* **349**, 153–161 (2015).

109. Friedrich, O. *et al.* Influence of test size, water depth, and ecology on Mg/Ca, Sr/Ca, $\delta^{18}\text{O}$ and $\delta^{13}\text{C}$ in nine modern species of planktic foraminifers. *Earth Planet. Sci. Lett.* **319–320**, 133–145 (2012).

110. Schmidt, G. A. Error analysis of paleosalinity calculations. *Paleoceanography* **14**, 422–429 (1999).

111. Ronay, E. R., Breitenbach, S. F. M. & Oster, J. L. Sensitivity of speleothem records in the Indian Summer Monsoon region to dry season infiltration. *Sci. Rep.* **9**, 5091 (2019).

112. Tipple, B. J., Berke, M. A., Doman, C. E., Khachaturyan, S. & Ehleringer, J. R. Leaf-wax n-alkanes record the plant-water environment at leaf flush. *Proc. Natl. Acad. Sci. USA* **110**, 2659–2664 (2013).

113. Hu, J., Emile-Geay, J., Tabor, C., Nusbaumer, J. & Partin, J. Deciphering oxygen isotope records from Chinese Speleothems with an isotope-enabled climate model. *Paleoceanogr. Paleoclimatol.* **34**, 2098–2112 (2019).

114. Konecky, B., Dee, S. G. & Noone, D. C. WaxPSM: a forward model of leaf wax hydrogen isotope ratios to bridge proxy and model estimates of past climate. *J. Geophys. Res. Biogeosci.* **124**, 2107–2125 (2019).
115. Thirumalai, K., Quinn, T. M. & Marino, G. Constraining past seawater $\delta^{18}\text{O}$ and temperature records developed from foraminiferal geochemistry. *Paleoceanography* **31**, 1409–1422 (2016).
116. Lüthi, D. et al. High-resolution carbon dioxide concentration record 650,000–800,000 years before present. *Nature* **453**, 379–382 (2008).
117. Dutton, A. et al. Phasing and amplitude of sea-level and climate change during the penultimate interglacial. *Nat. Geosci.* **2**, 355–359 (2009).
118. McFarlin, J. M. et al. Pronounced summer warming in northwest Greenland during the Holocene and Last Interglacial. *Proc. Natl Acad. Sci. USA* **115**, 6357–6362 (2018).
119. Laskar, J. et al. A long-term numerical solution for the insolation quantities of the Earth. *Astron. Astrophys.* **428**, 261–285 (2004).
120. Berger, A. & Loutre, M. F. Insolation values for the climate of the last 10 million years. *Quat. Sci. Rev.* **10**, 297–317 (1991).
121. Xie, P. & Arkin, P. A. Global precipitation: a 17-year monthly analysis based on gauge observations, satellite estimates, and numerical model outputs. *Bull. Am. Meteorol. Soc.* **78**, 2539–2558 (1997).

Acknowledgements

We thank H. Sloane for help with the stable isotope analysis and S.J. Hammond for help with trace-element analysis. Samples were provided by the IODP and we thank staff at the Kochi Core Centre (KCC). We appreciate comments from P.F. Sexton and thank I. Hall for early discussion of results. P.A. and K.N.-K. acknowledge funding through a NERC PhD grant (NE/L002493/1) associated with the CENTA Doctoral Training Partnership. Stable isotope analysis of planktic foraminifera was funded by NIGFSC (IP-1649-1116 and IP-1838-1118) and NERC (NE/M021181/1) grants to P.A. and P.B.H. (NE/P015093/1) acknowledges NERC funding support.

Author contributions

K.N.-K. and P.A. designed the project. K.N.-K. processed samples, generated data and compiled the proxy database. P.B.H. performed the climate model experiments. M.J.L. was responsible for the planktic foraminifera stable isotope analyses and S.C.C. provided

benthic foraminifera isotope data. K.N.-K., P.A. and P.B.H. wrote the manuscript with input from all co-authors.

Competing interests

The authors declare no competing interests.

Additional information

Supplementary information The online version contains supplementary material available at <https://doi.org/10.1038/s43247-021-00133-7>.

Correspondence and requests for materials should be addressed to K.N.-K.

Peer review information Primary handling editors: Sze Ling Ho, Heike Langenberg.

Reprints and permission information is available at <http://www.nature.com/reprints>

Publisher's note Springer Nature remains neutral with regard to jurisdictional claims in published maps and institutional affiliations.



Open Access This article is licensed under a Creative Commons Attribution 4.0 International License, which permits use, sharing, adaptation, distribution and reproduction in any medium or format, as long as you give appropriate credit to the original author(s) and the source, provide a link to the Creative Commons license, and indicate if changes were made. The images or other third party material in this article are included in the article's Creative Commons license, unless indicated otherwise in a credit line to the material. If material is not included in the article's Creative Commons license and your intended use is not permitted by statutory regulation or exceeds the permitted use, you will need to obtain permission directly from the copyright holder. To view a copy of this license, visit <http://creativecommons.org/licenses/by/4.0/>.

© The Author(s) 2021

Preflight Results

Document Overview

Title: Dipole patterns in tropical precipitation were pervasive across land and ocean
Author: Katrina Nilsson-Kerr
Creator: Springer
Producer: iText® 5.3.5 ©2000-2012 1T3XT BVBA (SPRINGER SBM; licensed version)

Legend: (X) - Can NOT be fixed by PDF/A-1b conversion.
(!X) - Could be fixed by PDF/A-1b conversion. User chose to be warned in PDF/A settings.

Page 1 Results

(X) Subsetted font DGHPNF+AdvOTea1a7398 does not define all referenced glyphs.

Page 2 Results

(X) Subsetted font DGHPNF+AdvOTea1a7398 does not define all referenced glyphs.

Page 3 Results

(X) Subsetted font DGHPNF+AdvOTea1a7398 does not define all referenced glyphs.

Page 4 Results

(X) Subsetted font DGHPNF+AdvOTea1a7398 does not define all referenced glyphs.

Page 5 Results

(X) Subsetted font DGHPNF+AdvOTea1a7398 does not define all referenced glyphs.

Page 6 Results

(X) Subsetted font DGHPNF+AdvOTea1a7398 does not define all referenced glyphs.

Page 7 Results

(X) Subsetted font DGHPNF+AdvOTea1a7398 does not define all referenced glyphs.

Page 8 Results

(X) Subsetted font DGHPNF+AdvOTea1a7398 does not define all referenced glyphs.

Page 9 Results

(X) Subsetted font DGHPNF+AdvOTea1a7398 does not define all referenced glyphs.